



Article

A Hollow-Shaped ZIF-8-N-Doped Porous Carbon Fiber for High-Performance Zn-Ion Hybrid Supercapacitors

Mingqi Wei ^{1,2}, Zhenlong Jiang ², Chengcheng Yang ², Tao Jiang ², Linlin Zhang ^{1,2}, Guangzhen Zhao ^{2,3,*} , Guang Zhu ^{1,2,*}, Lianghao Yu ² and Yuanyuan Zhu ²

¹ School of Mechanics and Optoelectronics Physics, Anhui University of Science and Technology, Huainan 232001, China; qiming202103@163.com (M.W.); llzhang156@163.com (L.Z.)

² Key Laboratory of Spin Electron and Nanomaterials of Anhui Higher Education Institutes, Suzhou University, Suzhou 234000, China; jzl5457@163.com (Z.J.); ycc151191@163.com (C.Y.); lhyu@ahsuzu.edu.cn (L.Y.)

³ State Key Laboratory of Biobased Material and Green Papermaking, Qilu University of Technology, Shandong Academy of Sciences, Jinan 250353, China

* Correspondence: zhaogzgold@126.com (G.Z.); guangzhu@ahsuzu.edu.cn (G.Z.);
Tel.: +86-0557-2871-036 (Guang Zhu)

Abstract: The advantages of low cost, high theoretical capacity, and dependable safety of aqueous zinc ion hybrid supercapacitors (ZHSCs) enable their promising use in flexible and wearable energy storage devices. However, achieving extended cycling stability in ZHSCs is still challenged by the limited availability of carbon cathode materials that can effectively pair with zinc anode materials. Here, we report a method for synthesising heteroatom-doped carbon nanofibers using electrostatic spinning and metal-organic frameworks (specifically ZIF-8). Assembled Zn // ZPCNF-1.5 ZHSCs exhibited 193 mA h g⁻¹ specific capacity at 1 A g⁻¹ and 162.6 Wh kg⁻¹ energy density at 841.2 kW kg⁻¹. Additionally, the device showed an ultra-long cycle life, maintaining 98% capacity after 20,000 cycles. Experimental analysis revealed an increase in the number of pores and active sites after adding ZIF-8 to the precursor. Furthermore, N doping effectively enhanced Zn²⁺ ions chemical adsorption and improved Zn-ion storage performance. This work provides a feasible design strategy to enhance ZHSC energy storage capability for practical applications.



Citation: Wei, M.; Jiang, Z.; Yang, C.; Jiang, T.; Zhang, L.; Zhao, G.; Zhu, G.; Yu, L.; Zhu, Y. A Hollow-Shaped ZIF-8-N-Doped Porous Carbon Fiber for High-Performance Zn-Ion Hybrid Supercapacitors. *Batteries* **2023**, *9*, 405. <https://doi.org/10.3390/batteries9080405>

Academic Editors: Lin Li and Changshin Jo

Received: 11 June 2023

Revised: 12 July 2023

Accepted: 30 July 2023

Published: 3 August 2023



Copyright: © 2023 by the authors. Licensee MDPI, Basel, Switzerland. This article is an open access article distributed under the terms and conditions of the Creative Commons Attribution (CC BY) license (<https://creativecommons.org/licenses/by/4.0/>).

1. Introduction

The in-depth studies of new devices of electrochemical energy storage have been promoted by the rapid development of flexible wearable intelligent electronics drives. As previously reported, traditional energy storage devices are too heavy and inflexible to support the portability and wearability of electronic devices [1–4]. To solve those problems in portable electronic devices, future energy storage devices are reported to have the characteristics of high energy density, high power density, superior mechanical properties, safety, and reliability [5–8]. Supercapacitors (SCs) are considered promising capacitors compared to other energy storage devices because of their high power density, stability, safety factor and fast charging and discharging. However, their practical application has been hindered to a certain extent by low energy density.

In recent years, to improve their energy density, researchers have paid increasing attention to hybrid SCs, which are based on monovalent (K⁺, Na⁺) or multivalent metal cations (Ca²⁺, Mg²⁺, Zn²⁺) [9–11], especially Zinc-ion hybrid SCs (ZHSCs) with the advantages of rich Zn content, safety, environmental protection and low cost. Besides, Zn anodes are reported to have the characteristics of substantial theoretical capacity, low working potential (−0.76 V vs standard hydrogen electrode (SHE)), reasonable cost, and inherent safety in aqueous solutions of electrolytes suggesting the great potential of ZHSCs for energy storage applications [12,13]. Studies have shown that Zinc anodes can provide

enough redox reaction during charge/discharge to match the maximum cathode capacity, thus endowing ZHSCs with higher energy density [14–18]. Porous carbon fiber materials are characterized by low cost and well electrical conductivity, and their use as cathode materials for ZHSCs has been explored. Reversible desorption and adsorption of SO_4^{2-} in internal pores or on cathode surfaces were confirmed to enhance the rate performance and cycle stability of ZHSCs [19,20]. However, carbon fibers usually have low porosity and surface area comparable to activated carbon, limiting their active substance loading, cyclic stability, and specific capacity. The material's surface provides a site for ion storage, so increasing the specific surface area (SSA) will improve the electrochemical performance of the material. Although the SiO_2 hard template was reported to enhance the surface area efficiently, template removal required the harmful hydrofluoric acid etching process. Studies have shown that heteroatomic modifications can provide additional pseudo-capacitance by promoting ion chemisorption [21–23]. For instance, introducing heteroatoms like N, O, S, etc., into carbon-based materials could modify the adsorption barrier, increase the electrode wettability, and endow the materials with more structural defects, thus improving capacitor storage performance and enable oxygen-enriched carbon fiber cathodes to achieve 97.7 Wh kg⁻¹/9.9 kW kg⁻¹ energy/power densities with high cycling stability [24–26]. This suggested the necessity to develop a facile and green modification method to obtain high-performance ZHSCs by optimizing nanofiber microstructures.

Metal-organic-frameworks (MOFs), such as MIL-47 [27] and MIL-88A [28], have the merits of tunable pore structure and high surface area and are recently applied in ZHSCs, leading to the synthesis and application of many MOFs-derived porous carbon materials or composites with higher conductivity to enhance ZHSC performance. However, ZHSC performance is often undermined by bulky solid particles induced by directly carbonizing conventional MOFs precursors.

In this study, based on the merits of structural tunability derived from MOFs as well as the outstanding electron/ion transport performance and structural integrity of carbon fibers [29,30], a zeolite imidazole skeleton of Zn (ZIF-8) derived N-doped porous carbon fiber (ZPCNF) was designed and prepared in combination with electrostatic spinning. The electrode incorporates a graded porous structure and N-doping with a large electrolyte contact area, rich active sites, and enhanced electron/ion transport kinetics. The ZHSCs with N-doped porous carbon fiber as the cathode and Zn foil as the anode delivered remarkable cycle stability and high performance.

2. Methods and Materials

2.1. Materials

The experimental materials included polyacrylonitrile (PAN, $M_w = 150,000$), N, N-Dimethylformamide (DMF, AR), 2-methylimidazole (AR), zinc nitrate ($\text{Zn}(\text{NO}_3)_2 \cdot 6\text{H}_2\text{O}$, AR), ethanol (AR), methanol (AR), hydrochloric acid (HCl, AR), and argon (Ar, high quality). The chemicals and reagents in the experiment as purchased without further purification.

2.2. Preparation of ZIF-8 and ZPCNF

Synthesis of ZIF-8 particles followed a previous method [31]. Briefly, $\text{Zn}(\text{NO}_3)_2 \cdot 6\text{H}_2\text{O}$ (2.975 g) was completely dissolved in 113 mL of methanol solution and defined as solution A. Then, solution B was prepared by dissolving 6.8 g of 2-methylimidazole completely in 113 mL of methanol solution, followed by mixing and stirring Solution A and B vigorously. After standing for 24 h, the mixed solution was transferred to a centrifuge tube for centrifugation. After washing with methanol, the white precipitate was dried for 12 h at 60 °C.

The spinning precursor solution was prepared by dispersing a certain amount of ZIF-8 in 10 mL of DMF under sonication and stirring, then adding 0.8 g of PAN and stirring for 12 h at 70 °C. Next, the suspension was electrospun using a single-nozzle syringe (10 mL) at 0.07 mL min⁻¹ flow rate, 16 kV DC voltage, 16 cm collection distance, 25 °C ambient

temperature and 30% relative humidity. Finally, the spun samples with specific thicknesses were obtained.

The ZPCNF preparation process is shown in Figure 1. The obtained electrospun fiber was heated for 2 h at $2\text{ }^{\circ}\text{C min}^{-1}$ to $300\text{ }^{\circ}\text{C}$, followed by carbonization for 2 h at $5\text{ }^{\circ}\text{C min}^{-1}$ to $1000\text{ }^{\circ}\text{C}$ in Ar atmosphere. After immersion in 6 mol L^{-1} HCl solution at $60\text{ }^{\circ}\text{C}$ for 12 h, the samples were washed repeatedly with deionized water and dried at $80\text{ }^{\circ}\text{C}$ for 12 h. Additionally, comparison samples were prepared by varying the ZIF-8 mass at 0 g (PCNF), 0.5 g (ZPCNF-0.5), 1.0 g (ZPCNF-1.0) and 1.5 g (ZPCNF-1.5).

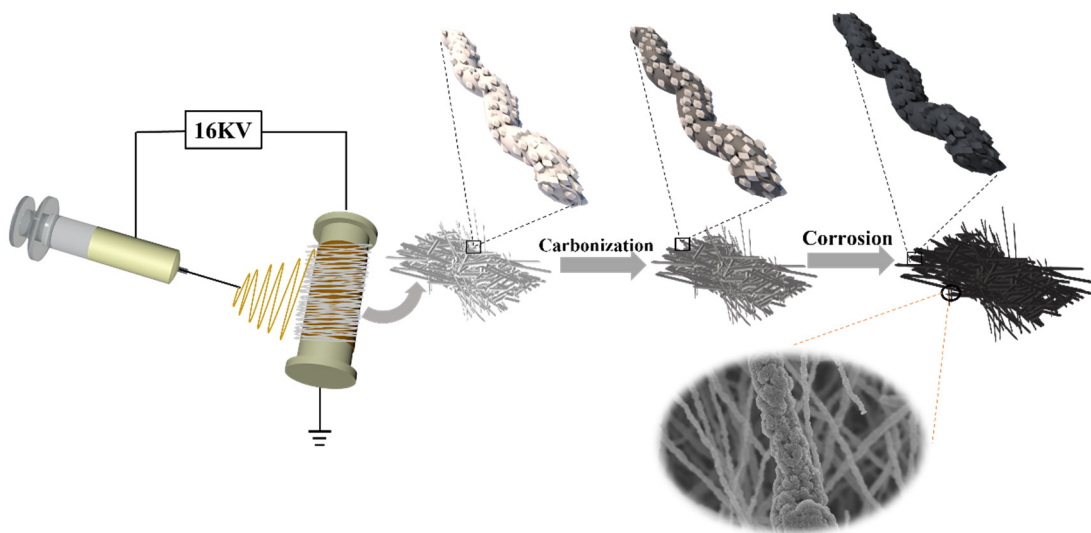


Figure 1. Schematic process diagram for ZPCNF preparation.

2.3. Physical Characterization

The morphology structure and element distribution of the samples were tested by field emission scanning electron microscope (SEM, Hitachi S-4800, 20 kV, 20 keV) equipped with energy dispersive spectrometer (EDS, Bruker Quantax-400, Billerica, MA, USA) and high-resolution transmission electron microscope (HRTEM, JEOL-2000, 200 kV, Akishima, Japan). X-ray diffractometer (XRD, Rigaku Smart Lab, Tokyo, Japan, TM 9 kW, Cu-K α , $\lambda = 1.5418\text{ \AA}$, 40 kV, 30 mA, scanning range 5–90°) and Raman spectrometer (Raman, Horiba Jobin Yvon 800, Kyoto, Japan, 10 mW, diffraction grating 600/1800 mm, the wavelength LASER excitation was equal to 532 nm) and Physical adsorption instrument (Micrometric, ASAP2020, Norcross, GA, USA) measurements of sample microstructure, SSA and pore distribution were performed using X-ray photoelectron spectroscopy (XPS, Escalab 250Xi, 150 W, X-ray beam spot 400 μm , using AlK α as the radiation source, a low energy flood-gun for charge compensation $h\nu = 1486.6\text{ eV}$) analyzed material element composition and valence states, and used XPS Peak 4.1 software to fit XPS test results. Shirley's baseline was used as a background.

2.4. Electrochemical Measurements

The working electrodes are made by combining 80 wt. % of ZPCNF-x material with 10 wt. % of acetylene black and 10 wt. % of polyvinylidene fluoride (PVDF) in N-methyl pyrrolidone (NMP) solution, a loading of approximately $1.0\text{--}2.0\text{ mg cm}^{-2}$. The electrolyte was in 2 M ZnSO_4 aqueous solution. The ZHSCs were obtained by taking Zn as the anode and ZPCNF-x as the cathode (working electrodes). The cyclic voltammetry (CV, 2 to 100 mV s^{-1} , a voltage range of 0.1–2.0 V) and Galvanostatic charge–discharge tests (GCD, 0.1 to 20 A g^{-1}) were performed on the Corrtest electrochemical workstation (CS2350H). And the long-cycle stability of ZHSCs on the Neware test system.

3. Results and Discussion

The schematic ZPCNF synthetic process is presented in Figure 1. ZIF-8 and PAN were combined by electrostatic spinning to form organic ligands. After carbonization at 1000 °C in the Ar atmosphere, ZIF-8 nanoparticles were inlaid with N-doped carbon fiber materials, coupled with partial volatilization of Zn^{2+} species in ZIF-8 particles in the form of metallic Zn reduction at high temperature, enabling many pores in carbon fibers. The SSA was increased by additional etching in hydrochloric acid to remove excess zinc monomers. The interconnection of ZIF-8 particles allowed the formation of layered porous nanofibers. The nitrogen of dimethylimidazole during carbonization also contributed to a small increase in the fiber nitrogen content.

The embedding of ZIF-8 particles in the electrospinning solution altered the structure and morphology of the derived electrospinning fibers and carbonized products. The SEM images of PCNF, ZPCNF-0.5, ZPCNF-1.0 and ZPCNF-1.5 can be seen in Figures S1 and 2. In Figures S1a,b and 2a, the as-prepared PCNF was shown to have a fibrous network structure with clear massive nodes, a very smooth surface and many fracture points, with no obvious pore distribution on the fiber surface. In the SEM images of Figure S1c–h, a clear network structure with a rough carbon nanofiber surface could be observed in ZPCNF-0.5, ZPCNF-1.0 and ZPCNF-1.5, and compared with PCNF, ZPCNF-0.5, ZPCNF-1.0, and ZPCNF-1.5 exhibited no agglomeration or fractured nodes as shown in Figure S1. Meanwhile, many pore structures could be observed on the surface of ZPCNF-0.5, ZPCNF-1.0 and ZPCNF-1.5, favoring rapid electrolyte ions transport and diffusion in the subsequent charge and discharge process. In the SEM images of Figure 2b,c, ZPCNF-0.5 and ZPCNF-1.0 exhibited a similar structure, with an uneven distribution of pore structures. In Figures S1g,h and 2d, ZPCNF-1.5 was seen to have no fracture nodes, with a rich pore structure and 3D network structure.

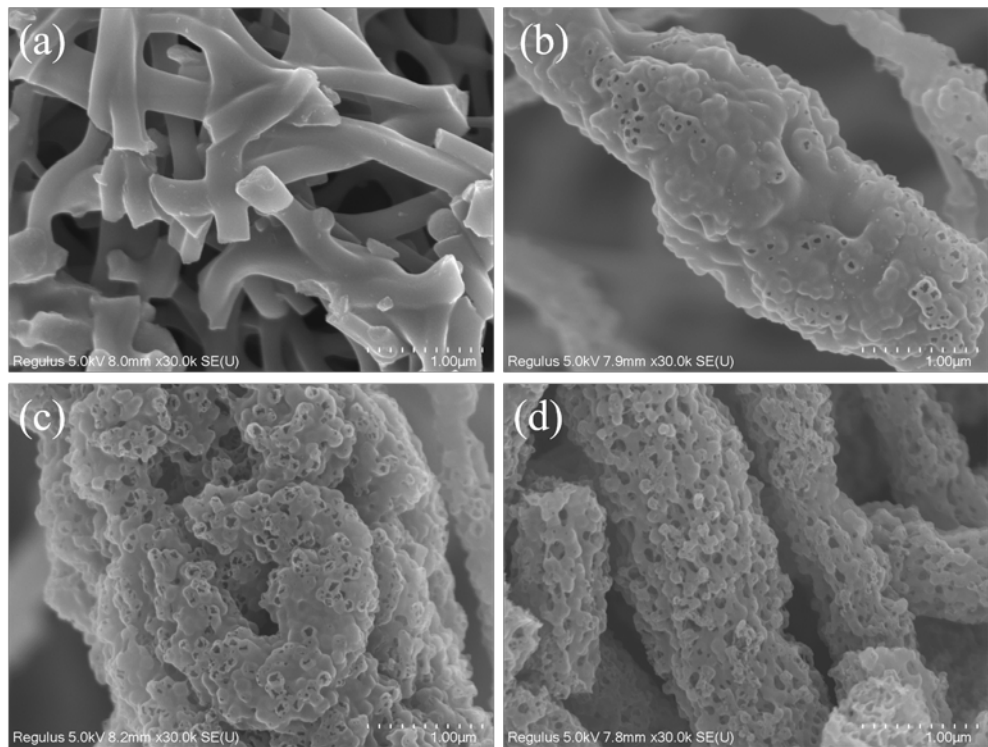


Figure 2. SEM images of PCNF (a), ZPCNF-0.5 (b), ZPCNF-1.0 (c) and ZPCNF-1.5 (d).

The inner pore structure of ZPCNF-1.5 was analyzed by TEM and HRTEM, displayed in Figure 3. In Figure 3a,b, the fiber of ZPCNF-1.5 was seen to have a diameter of about 1 μm , and consist of various 70-to-100 nm-diameter hollow particles connected by carbon matrix, indicating the post-carbonization transformation of ZIF-8 particles to a hollow structure. In

Figure 3b, the carbon nanofibers of ZPCNF-1.5 were observed to be almost transparent-like, suggesting the existence of a rich porous structure. The HRTEM image of ZPCNF-1.5 is shown in Figure 3c, where no characteristic lattice fringes could be observed. By further analysis of the selected area electron diffraction (SAED) image in the inset of Figure 3c, the vague rings of the SAED pattern and the disordered lattice spacing revealed the amorphous carbon structure in the porous carbon fiber [32,33]. It also partly reflects the material's high SSA and good electrochemical stability [34]. The elemental composition of ZPCNF-1.5 carbon nanofibers was investigated by SEM and elemental mapping, and in Figure 3d, C, N and O were shown to be uniformly distributed without evident aggregation, indicating the successful incorporation of N and O atoms into carbon fibers. The residual cavities, porous structures and N and O atoms doping of ZPCNF-1.5 can promote electrolyte permeation, ions diffusion and accommodation of volume changes during the discharge-charge process.

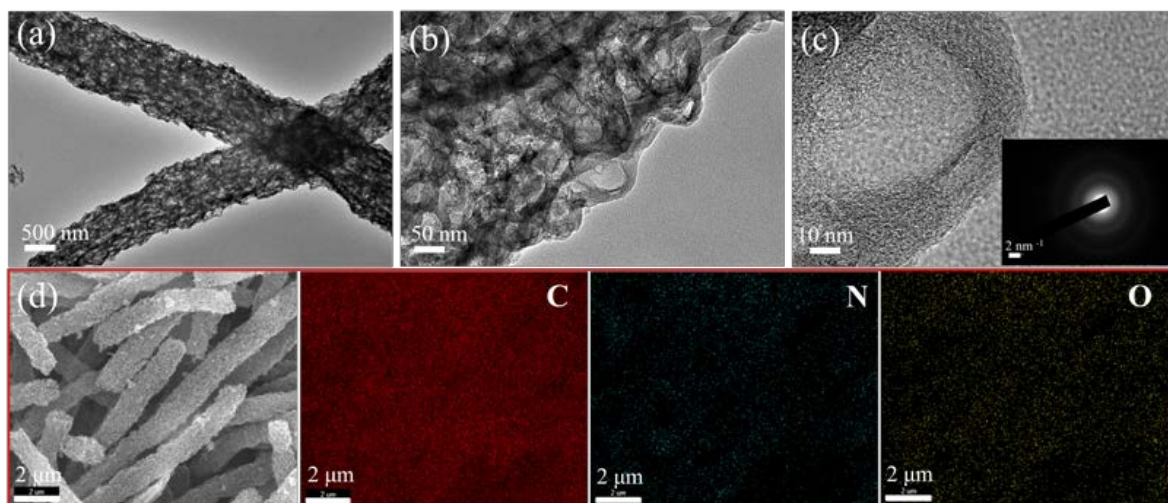


Figure 3. TEM (a,b), and HRTEM (c) images of ZPCNF-1.5, with the inset of (c) for the selected area electron diffraction (SAED) image of ZPCNF-1.5. Elemental mappings of C, N, O in ZPCNF-1.5 (d).

The crystal structure of PCNF, ZPCNF-0.5, ZPCNF-1.0 and ZPCNF-1.5 materials was investigated by XRD measurements. As shown in Figure 4a, all samples have a broad peak around 25° , corresponding to graphite's (002) crystal plane. The weak peak near 43° can be attributed to the 100 peak, which reflects the amorphous structure and is consistent with the SAED picture (Figure 3c) [35–37]. Moreover, Zinc-related substances failed to be observed in the diffraction pattern, suggesting the complete removal of Zinc-related substances by high-temperature carbonization and pickling. The Raman spectra for the ZPCNF-1.5 in Figure 4b show the D and G bands at 1350 and 1580 cm^{-1} , respectively. The D band is derived from structural defects and disorder-induced features on carbon [38], and the G-band is ascribed to amorphous sp^2 -bonded carbon [39]. Its intensity ratio of the D peak to the G peak (I_D/I_G) is also calculated. The fitting area ratio of I_D/I_G values reflects the degree of disordering of carbonaceous materials. [40–43] Meanwhile Lorentz line was used to fit the Raman spectrum of PCNF, PCNF-0.5, and ZPCNF-1.0, provided in and Figures 4b and S2. The integrated area values of the D and G peaks are listed in Table S2 of the Supporting Information. Generally, the higher the I_D/I_G value, the higher the degree of disorder of the carbon material is reflected. As shown in Table S2, the I_D/I_G values are 2.78, 2.87, 3.26 and 3.38 for PCNF, ZPCNF-0.5, ZPCNF-1.0, and ZPCNF-1.5, respectively. And the above Raman results demonstrate that the ZPCNF-1.5 is more disordered than PCNF, PCNF-0.5, and ZPCNF-1.0, consistent with the XRD and the HRTEM in Figure 3. Due to a higher Zinc ion content ZPCNF-1.5 than the other fibers, more defect sites are formed after carbonization, leading to a significantly higher I_D/I_G value ZPCNF-1.5 than the other materials. The increase of defect sites is conducive to the rise of SSA in carbon materials,

forming more electrolyte ion adsorption and desorption active sites, thus improving the material-specific capacity.

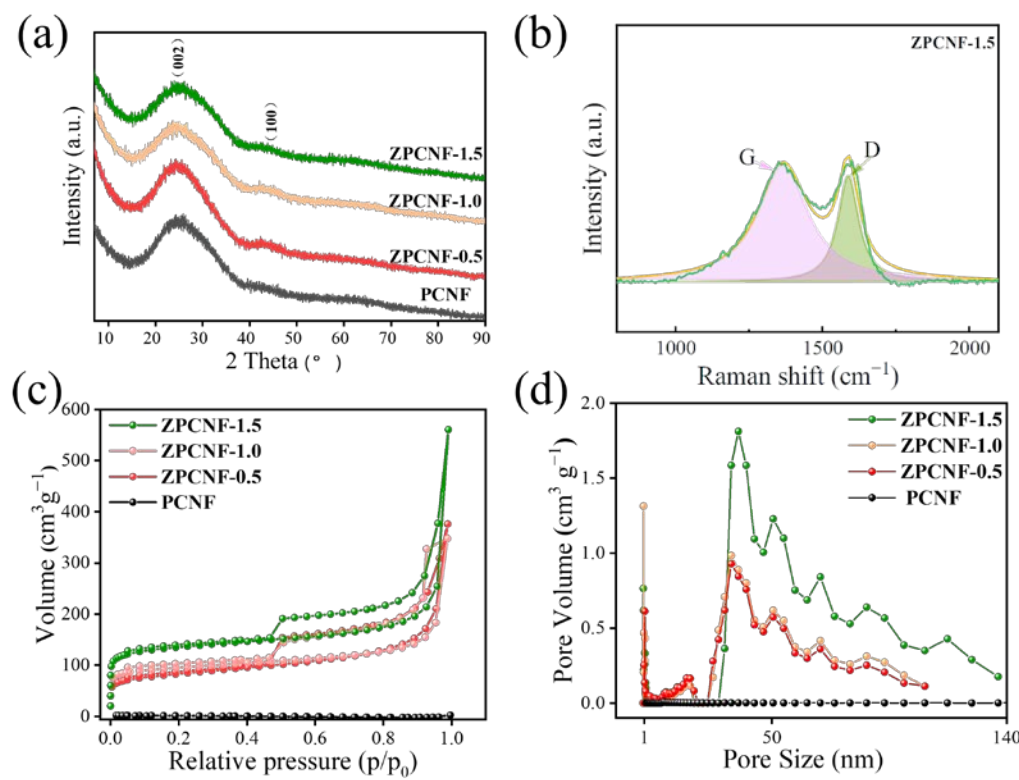


Figure 4. XRD patterns (a), Raman spectra (b), N_2 adsorption/desorption isotherms (c), and pore size distribution (d) of PCNF, ZPCNF-0.5, ZPCNF-1.0 and ZPCNF-1.5.

N_2 adsorption isotherms were examined at 77 K using a Micromeritics ASAP 2020 analyzer. SSA was obtained by Brunauer-Emmett-Teller (BET) theory, and the pore size distribution curves were determined by the density functional theory (DFT) method. Meanwhile, The model is based on the N2-DFT model. Figure 4c displays the N_2 -adsorption and desorption isotherms, where the N_2 isotherm of PCNF was attributed to a typical Type-I structure, reflecting that the pore structure of ZPCNF is dominated by micropores [44]. In contrast, strong adsorption ($P/P_0 < 0.05$), hysteresis ($P/P_0 > 0.5$), and broadened knees ($0.05 < P/P_0 < 0.5$) can be observed in the N_2 adsorption–desorption isotherms of ZPCNF-0.5, ZPCNF-1.0, and ZPCNF-1.5, demonstrating the presence of micropores and mesopores [45,46]. These mesopores could shorten diffusion distance and accelerate the fast adsorption/desorption of Zn^{+} ions. The N_2 adsorption–desorption isotherm of ZPCNF-1.5 exhibited a strong N_2 adsorption capacity ($P/P_0 < 0.05$), suggesting the presence of abundant microporous structures, which can provide abundant Zn^{2+} ion adsorption active sites. BET models were used to analyze the parameters of pore volume and specific surface area (S_{BET}), and the results are shown in Table S2. The specific surface areas (S_{BET}) values of PCNF, ZPCNF-0.5, ZPCNF-1.0 and ZPCNF-1.5 are 2.9 , 268.4 , 301.9 and $418.3 \text{ m}^2 \text{ g}^{-1}$, with corresponding pore volume of 0.0029 , 0.27 , 0.29 , and $0.33 \text{ cm}^3 \text{ g}^{-1}$, respectively. The PCNF produced by electrospinning and carbonization without adding ZIF-8 exhibited an extremely low SSA. After adding ZIF-8, the SSA of carbon nanofibers showed a ZIF-8 amount-dependent increase in the spinning solution precursor. The S_{BET} and pore volume of ZPCNF-1.5 ($418.3 \text{ m}^2 \text{ g}^{-1}$) was the highest of all the materials. In Figure 4d, the pore size distribution plots of PCNF showed a minimal porous structure, in contrast to a rich microporous structure, mesoporous structure, and macroporous structure ($>50 \text{ nm}$) in the pore size distribution plots of ZPCNF-0.5, ZPCNF-1.0 and ZPCNF-1.5. These graded

porous structures can provide abundant electrolyte ions adsorption sites and transport channels for rapid ions transport.

The surface element composition and atomic valence state of PCNF, ZPCNF-0.5, ZPCNF-1.0 and ZPCNF-1.5 were analyzed by X-ray photoelectron spectroscopy (XPS). As shown in Figure 5a, PCNF, ZPCNF-0.5, ZPCNF-1.0 and ZPCNF-1.5 exhibited prominent O 1s and N 1s peaks, indicating that their surfaces are abundant in N and O elements, which can enhance their capacitive properties. Additionally, the elements of N and O can provide pseudo-capacitance while enhancing the substance's hydrophilicity. The results of the fits to the high-frequency O1s peaks of all samples are shown in Figures 5b and S2a–c, where the O1s peaks can be fitted to three different forms of O. The 530.6 eV peak represents the O atom in the C=O structure, while the other peaks are at 533.2 eV and 534.4 eV, with the 534.4 eV peak for the presence of O in the C-OH structure, while the 533.2 eV peak for the O atom in the C-O structure [47]. The N1s region spectra (Figures 5c and S3d–f) can be fitted to four forms of N, pyrrolic nitrogen (N-5), pyridinic nitrogen (N-6), graphitic nitrogen (N-Q), and nitrogen oxide (N-X). N-5 and N-6 are the main N-containing functional groups, active sites during electrochemical processes. N-X, N-5, and N-6 can be reversibly switched between different morphologies, providing certain pseudo-capacitance for carbon materials. Moreover, N-Q was reported to improve the carbon fiber electrical conductivity by supplying more free electrons in the carbon structure [48].

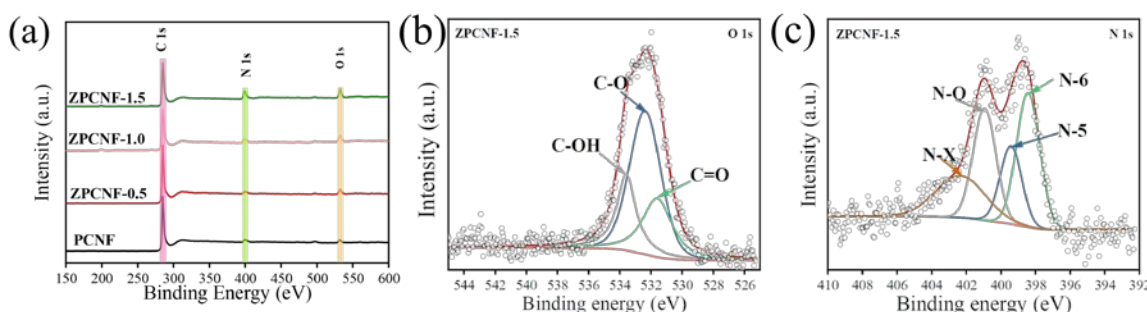


Figure 5. XPS survey spectra (a) of PCNF, ZPCNF-0.5, ZPCNF-1.0, and ZPCNF-1.5. High-resolution O1s spectrum (b) and N1s spectrum (c) of ZPCNF-1.5.

The carbon electrode electrochemical performance was investigated by assembling ZHSCs using carbon electrodes as cathodes, commercial Zn foils as anodes, and 2.0 M ZnSO₄ aqueous solution as electrolyte. A representative ZPCNF-1.5 was used as the carbon electrode to test the cyclic voltammetry (CV) curves at different voltage windows and a scan rate of 10 mV s⁻¹. As shown in Figure 6a, the CV curves displayed rectangular shapes for the CV curve with 0.1–2.1 V voltage window, and a small polarization peak appeared, attributed to a slow oxygen evolution reaction (OER). In Figure 6b, the galvanostatic charge-discharge (GCD) curves at 1 A g⁻¹ were shown to have an obvious voltage drop at discharge onset for voltage windows above 2.0 V. With voltage window expanded from 0.1–2.0 V to 0.1–2.1 V, the overall specific capacitance has increased significantly. This is due to the improved capacitive behavior and the additional OER., in contrast to a decrease of Coulombic efficiency from 100% to 91% (Figure 6c). Accordingly, an operating voltage of 0.1–2.0 V was selected for the assembled ZHSCs.

The application of PCNF, ZPCNF-0.5, ZPCNF-1.0 and ZPCNF-1.5 was evaluated first by measuring their CV and GCD in 2 M ZnSO₄ electrolyte with 0.1–2.0 V voltage window, and the results are presented in Figures 7, S4 and S5. In Figures 7a and S4, similar shapes can be observed in the CV curves at various scan rates, suggesting fast charge storage kinetics and outstanding rate performance even at a high scan rate. GCD was measured at 1–20 A g⁻¹ current density, and the results are shown in Figures S5 and 7b, which are shown a similar shape in the GCD curves at different current densities. In Figure 7c, all the CV curves at the 20 mV s⁻¹ scan rate exhibited a rectangular shape. At about 0.9/1.1 V, small cathodic/anodic humps could be observed, suggesting a redox reaction in the energy

storage of ZHSCs. ZPCNF-1.5 showed a relatively larger cathodic/anodic hump and enclosed area among them. Figure 7d shows the GCD curves at 1 A g^{-1} current density, and ZPCNF-1.5 was seen to exhibit a larger discharge time in the GCD curve, indicating a larger specific capacitance of ZPCNF-1.5 than PCNF, ZPCNF-0.5 or ZPCNF-1.0.

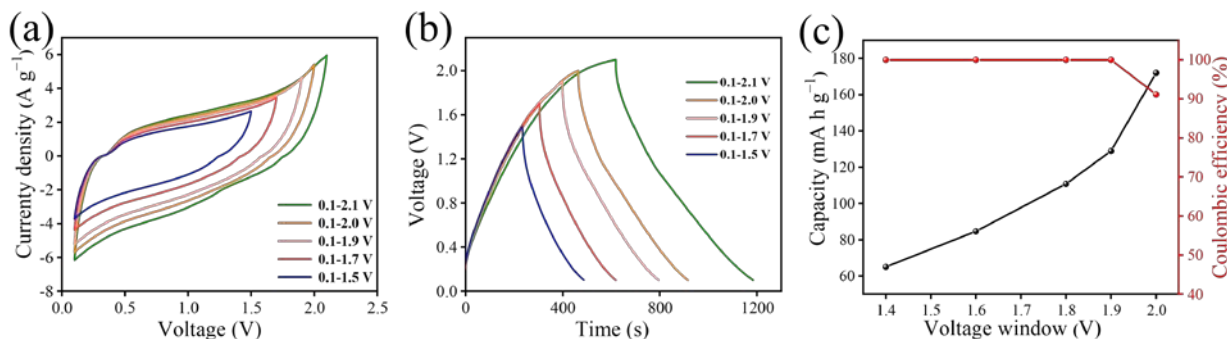


Figure 6. CV curves with different voltage windows for ZPCNF-1.5 (10 mV s^{-1}) (a). GCD curves with varying voltage windows (1 A g^{-1}) (b). Specific capacities and Coulombic efficiency derived from GCD curves (c).

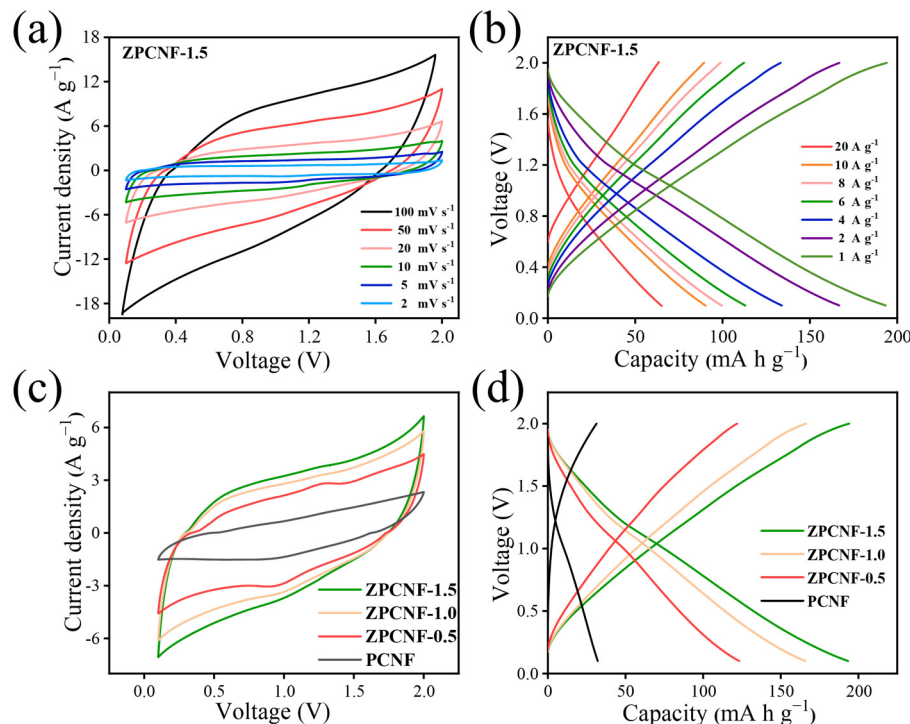


Figure 7. CV curves of ZPCNF-1.5 at various scan rates (a), GCD curves at various current densities (b), and CV curves at 20 mV s^{-1} (c), and GCD curves at 1 A g^{-1} (d) for PCNF, ZPCNF-0.5, ZPCNF-1.0 and ZPCNF-1.5.

The Dunn method was employed to analyze the contribution of pseudocapacitive behavior. The diffusion-controlled and capacitive charge storage processes are described by Equation (S4) [49,50]. In Figure 8a, the capacitive contribution percentage was seen to increase to 17.78%, 22%, 27.24%, 35.65%, and 56.14% at 2, 5, 10, 20, and 50 mV s^{-1} , respectively, demonstrating the rapid charge storage kinetics in the cathode, with a low redox process controlled by diffusion. With the increase in scan rate, the dynamic process of ZPCNF-1.5 gradually changed from diffusion-controlled behavior to capacitance-controlled behavior. Based on GCD measurement results, the corresponding specific capacitances at different current densities were obtained for PCNF, ZPCNF-0.5, ZPCNF-1.0 and ZPCNF-1.5 electrodes (Figure 8b). With the rise of current density, the specific capacitance of

capacitors showed a downtrend, with the highest specific capacitance for ZPCNF-1.5 at any current density. At 1 A g^{-1} current density, the specific capacitances were 32, 123, 165 and 193 mA h g^{-1} for PCNF, ZPCNF-0.5, ZPCNF-1.0 and ZPCNF-1.5, respectively. The specific capacity of ZPCNF-1.5 could reach 193 mA h g^{-1} at 1 A g^{-1} current density while remaining at 65 mA h g^{-1} at 20 A g^{-1} current density. This indicated a ZIF-8 amount-dependent increase in the capacity of the material, which is related to the most significant SSA of ZPCNF-1.5 and the ability of N and O doping. Figure 8c shows the Ragone diagram of ZPCNF-1.5 derived from the GCD test results [26,51–57]. At 841.2 W kg^{-1} power density, the energy density was 162.6 Wh kg^{-1} . At 12.2 kW kg^{-1} output power density, 40 Wh kg^{-1} energy density could still be maintained, reflecting the outstanding rate performance and relatively high energy density of ZPCNF-1.5. The cycle stability of Zn//ZPCNF-1.5 ZHSCs was further investigated at 10 A g^{-1} current density. As shown in Figure 8d, ZPCNF-1.5 also exhibited high cycling stability after 20,000 cycles, retaining 98% capacity and achieving nearly 100% Coulombic efficiency. After about 16,000 cycles, capacity retention dropped to 95.5% and returned to its original value after replacing the zinc anode. This indicated that the material has good cycling stability, and the drop in capacity retention is induced by the development of zinc dendrites during zinc anode degradation. Meanwhile, as shown in the inset of Figure 8d, the device of Zn//ZPCNF-1.5 ZHSCs could drive a “SZU” logo formed of 49 blue light-emitting diode (LED) lamps in parallel, demonstrating its practical application potential. Then Figure S6 displays the self-discharge curves of Zn//ZPCNF-1.5 ZHSCs, from which a sharp decline followed by flattening out can be seen. The voltage of Zn//ZPCNF-1.5 ZHSCs started to drop sharply from 2 to 1.5 V within 4 h, which was followed by a slow self-discharge process that resulted in a retained potential of 1.48 V even after 24 h, which means that Zn//ZPCNF-1.5 ZHSCs possesses preferable anti-self-discharge property to some extent.

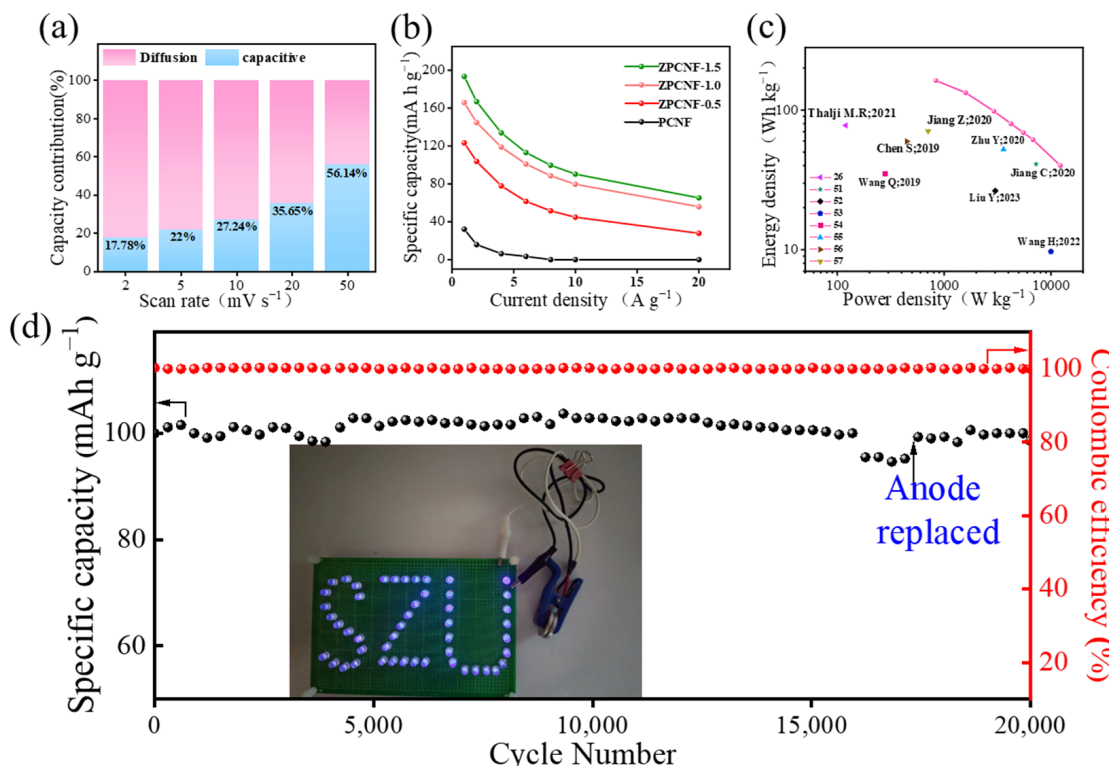


Figure 8. Capacitive contributions estimated by Dunn’s method (a) and Specific capacitances of PCNF, ZPCNF-0.5, ZPCNF-1.0 and ZPCNF-1.5 at different current densities (b). Ragone plots of ZPCNF-1.5 and some related literature reports (c) and Cycling performance at 10 A g^{-1} current density and Coulombic efficiency(d).

4. Conclusions

This work proposed an efficient method for producing N-doped carbon nanofibers with a hollow shape by combining PAN and ZIF-8 to prepare electrospun fibers followed by a simple carbonization treatment. The electrochemical performance of the produced N-doped carbon nanofibers in Zn-ion capacitors was investigated by varying ZIF-8 amount in the spinning precursor solution. ZPCNF-1.5 exhibited a 3D fibrous network structure, a huge SSA of $418.3 \text{ m}^2 \text{ g}^{-1}$ (much larger than that of PCNF, $2.9 \text{ m}^2 \text{ g}^{-1}$), graded porous structures (macropores, mesopores and micropores) and N and O heteroatom doping, displaying a specific capacitance of 193 mA h g^{-1} , an energy density of 162.6 Wh kg^{-1} , a power density of 841.2 W kg^{-1} . After 20,000 cycles, ZPCNF-1.5 retained high cycling stability with 98% capacity retention and a nearly 100% coulombic efficiency. The developed ZPCNF-1.5 electrode material has great application potential in Zn-ion capacitors.

Supplementary Materials: The following supporting information can be downloaded at: <https://www.mdpi.com/article/10.3390/batteries9080405/s1>, Material characterization; Electrochemical measurement; Calculation; Figure S1: SEM images of PCNF (a,b), ZPCNF-0.5 (c,d), ZPCNF-1.0 (e,f) SEM images of ZPCNF-1.5 (g,h); Figure S2: Raman spectra of the obtained PCNF, ZPCNF-0.5, and ZPCNF-1.0; Figure S3: High-resolution O 1s, N1s spectra of PCNF (a,d), ZPCNF-0.5 (b,e), ZPCNF-1.0 (c,f); Figure S4: The CV curves of PCNF (a), ZPCNF-0.5 (b), ZPCNF-1.0 (c); Figure S5: The GCD curves of PCNF (a), ZPCNF-0.5 (b), ZPCNF-1.0 (c); Figure S6: Self-discharge curves of Zn//ZPCNF-1.5 ZHSCs within the potential windows of 0.1–2.0 V; Table S1: The integral area values of D and G peaks of the obtained samples measured from Raman results; Table S2: Specific surface areas and pore volume of PCNF, ZPCNF-0.5, ZPCNF-1.0 and ZPCNF-1.5.

Author Contributions: Conceptualization, M.W. and G.Z. (Guangzhen Zhao); methodology, Z.J.; software, L.Z.; validation, T.J. and C.Y.; formal analysis, Y.Z.; writing—review and editing, L.Y.; writing—original draft preparation, G.Z. (Guang Zhu). All authors have read and agreed to the published version of the manuscript.

Funding: We gratefully acknowledge the financial support by the Foundation (No. GZKF202211) of State Key Laboratory of Biobased Material and Green Papermaking, the Scientific Research Foundation of Suzhou University (2016XJXS05 and 2018S2XYDZXZ02), Qilu University of Technology, Shandong Academy of Sciences, the Doctor of Suzhou University Scientific Research Foundation Project (2020BS015, 2020BS014), the Key Scientific Research Project of Suzhou University (2019yzd03), the Innovative Research Team of Anhui Provincial Education Department (2016SCXPTTD), the Natural Science Research Project in Universities of Anhui Province in China (KJ2020A0727), the Outstanding Youth Talents in Anhui Provincial Education Department (2017GXBZD47) and Key Discipline of Material Science and Engineering of Suzhou University (2017XJZDXK3), the Support Program for Excellent Young Talents in Universities of Anhui Province (Grant No. 2022AH030134, the Support Project of Universities for Young Talents under Grant of Anhui Province (GXYQ2021220, gxyq2020059)), Primary Research and Development Program of the Project of Anhui Province Academic and Technical Leader (2020D250).

Data Availability Statement: The data presented in this study are available on request from the corresponding author.

Conflicts of Interest: The authors declare no conflict of interest.

References

1. Zhao, R.; Elzatahry, A.; Chao, D.; Zhao, D. Making MXene more energetic in aqueous battery. *Matter* **2022**, *5*, 8–10. [[CrossRef](#)]
2. Xu, L.; Pan, G.; Yu, C.; Li, J.; Gong, Z.; Lu, T.; Pan, L. Co-doped MnO₂ with abundant oxygen vacancies as a cathode for superior aqueous magnesium ion storage. *Inorg. Chem. Front.* **2023**, *10*, 1748–1757. [[CrossRef](#)]
3. Zhao, R.; Di, H.; Hui, X.; Zhao, D.; Wang, R.; Wang, C.; Yin, L. Self-assembled Ti₃C₂ MXene and N-rich porous carbon hybrids as superior anodes for high-performance potassium-ion batteries. *Energy Environ. Sci.* **2020**, *13*, 246–257. [[CrossRef](#)]
4. Li, L.; Lu, Y.; Zhang, Q.; Zhao, S.; Hu, Z.; Chou, S.L. Recent progress on layered cathode materials for nonaqueous rechargeable magnesium batteries. *Small* **2021**, *17*, 1902767. [[CrossRef](#)]
5. Molaiyan, P.; Reis, G.D.; Karuppiah, D.; Subramaniyam, C.M.; García-Alvarado, F.; Lassi, U. Recent progress in biomass-derived carbon materials for Li-ion and Na-ion batteries—A review. *Batteries* **2023**, *9*, 116. [[CrossRef](#)]
6. Simon, P.; Gogotsi, Y. Perspectives for electrochemical capacitors and related devices. *Nat. Mater.* **2020**, *19*, 1151–1163. [[CrossRef](#)]

7. Yan, J.; Liu, T.; Liu, X.; Yan, Y.; Huang, Y. Metal-organic framework-based materials for flexible supercapacitor application. *Coord. Chem. Rev.* **2022**, *452*, 214300. [[CrossRef](#)]
8. Xie, B.; He, J.; Sun, Y.; Li, S.; Li, J. Hybrid Anionic Electrolytes for the High Performance of Aqueous Zinc-Ion Hybrid Supercapacitors. *Energies* **2022**, *16*, 248. [[CrossRef](#)]
9. Chao, D.; Zhou, W.; Ye, C.; Zhang, Q.; Chen, Y.; Gu, L.; Davey, K.; Qiao, S. An Electrolytic Zn-MnO₂ Battery for High-Voltage and Scalable Energy Storage. *Angew. Chem. Int. Ed. Engl.* **2019**, *58*, 7823–7828. [[CrossRef](#)]
10. Deng, X.; Li, J.; Zhu, S.; Sha, J.; Ma, L.; Zhao, Z. N. O co-doped hierarchical carbon cathode for high-performance Zn-ion hybrid supercapacitors with enhanced pseudocapacitance. *J. Mater. Chem. A* **2020**, *8*, 11617–11625. [[CrossRef](#)]
11. Pan, G.; Li, J.; Han, L.; Peng, W.; Xu, X.; Lu, T.; Amin, M.A.; Yamauchi, Y.; Xu, M.; Pan, L. MoS₂ nanosheets with expanded interlayer spacing for ultra-stable aqueous Mg-ion hybrid supercapacitor. *Inorg. Chem. Front.* **2022**, *9*, 1666–1673. [[CrossRef](#)]
12. Zeng, Y.; Zhang, X.; Qin, R.; Liu, X.; Fang, P.; Zheng, D.; Tong, Y.; Lu, X. Dendrite-Free Zinc Deposition Induced by Multifunctional CNT Frameworks for Stable Flexible Zn-Ion Batteries. *Adv. Mater.* **2019**, *31*, e1903675. [[CrossRef](#)] [[PubMed](#)]
13. Song, P.; Li, C.; Zhao, N.; Ji, Z.; Zhai, L.; Shen, X.; Liu, Q. Molten salt-confined pyrolysis towards heteroatom-doped porous carbon nanosheets for high-energy-density Zn-ion hybrid supercapacitors. *Colloid Interface Sci.* **2023**, *633*, 362–373. [[CrossRef](#)] [[PubMed](#)]
14. Li, Z.; An, Y.; Dong, S.; Chen, C.; Wu, L.; Sun, Y.; Zhang, X. Progress on zinc ion hybrid supercapacitors: Insights and challenges. *Energy Storage Mater.* **2020**, *31*, 252–266. [[CrossRef](#)]
15. Sui, D.; Wu, M.; Shi, K.; Li, C.; Lang, J.; Yang, Y.; Zhang, X.; Yan, X.; Chen, Y. Recent progress of cathode materials for aqueous zinc-ion capacitors: Carbon-based materials and beyond. *Carbon* **2021**, *185*, 126–151. [[CrossRef](#)]
16. Tang, B.; Shan, L.; Liang, S.; Zhou, J. Issues and opportunities facing aqueous zinc-ion batteries. *Energy Environ. Sci.* **2019**, *12*, 3288–3304. [[CrossRef](#)]
17. Wang, Y.; Zhang, L.; Zhang, F.; Ding, X.; Shin, K.; Tang, Y. High-performance Zn-graphite battery based on LiPF₆ single-salt electrolyte with high working voltage and long cycling life. *J. Energy Chem.* **2021**, *58*, 602–609. [[CrossRef](#)]
18. Zhang, N.; Chen, X.; Yu, M.; Niu, Z.; Cheng, F.; Cheng, J. Materials chemistry for rechargeable zinc-ion batteries. *Chem. Soc. Rev.* **2020**, *49*, 4203–4219. [[CrossRef](#)]
19. Huang, J.; Wang, L.; Peng, Z.; Peng, M.; Li, L.; Tang, X.; Xu, Y.; Tang, L.; Yuan, K.; Chen, Y. Minimization of ion transport resistance: Diblock copolymer micelle derived nitrogen-doped hierarchically porous carbon spheres for superior rate and power Zn-ion capacitors. *J. Mater. Chem. A* **2021**, *9*, 8435–8443. [[CrossRef](#)]
20. Han, L.; Zhang, X.; Li, J.; Huang, H.; Xu, X.; Liu, X.; Yang, Z.; Xu, M.; Pan, L. Enhanced energy storage of aqueous zinc-carbon hybrid supercapacitors via employing alkaline medium and B, N dual doped carbon cathode. *J. Colloid Interface Sci.* **2021**, *599*, 556–565. [[CrossRef](#)]
21. Feng, J.; Wang, Y.; Xu, Y.; Sun, Y.; Tang, Y.; Yan, X. Ion regulation of ionic liquid electrolytes for supercapacitors. *Energy Environ. Sci.* **2021**, *14*, 2859–2882. [[CrossRef](#)]
22. Wang, C.; Pei, Z.; Meng, Q.; Zhang, Z.; Sui, X.; Yuan, Z.; Wang, S.; Chen, Y. Toward Flexible Zinc-Ion Hybrid Capacitors with Superhigh Energy Density and Ultralong Cycling Life: The Pivotal Role of ZnCl₂ Salt-Based Electrolytes. *Angew. Chem. Int. Ed. Engl.* **2021**, *60*, 990–997. [[CrossRef](#)] [[PubMed](#)]
23. Chen, C.; Zhao, M.; Cai, Y.; Zhao, G.; Xie, Y.; Zhang, L.; Zhu, G.; Pan, L. Scalable synthesis of strutted nitrogen doped hierarchical porous carbon nanosheets for supercapacitors with both high gravimetric and volumetric performances. *Carbon* **2021**, *179*, 458–468. [[CrossRef](#)]
24. Peng, H.; Yao, B.; Wei, X.; Liu, T.; Kou, T.; Xiao, P.; Zhang, Y.; Li, Y. Pore and Heteroatom Engineered Carbon Foams for Supercapacitors. *Adv. Energy Mater.* **2019**, *9*, 1803665. [[CrossRef](#)]
25. Wei, J.; Ding, C.; Zhang, P.; Ding, H.; Niu, X.; Ma, Y.; Li, C.; Wang, Y.; Xiong, H. Robust Negative Electrode Materials Derived from Carbon Dots and Porous Hydrogels for High-Performance Hybrid Supercapacitors. *Adv. Mater.* **2019**, *31*, e1806197. [[CrossRef](#)]
26. Thalji, M.R.; Ali, G.A.; Liu, P.; Zhong, Y.; Chong, K. W18O49 nanowires-graphene nanocomposite for asymmetric supercapacitors employing AlCl₃ aqueous electrolyte. *Chem. Eng. J.* **2021**, *409*, 128216. [[CrossRef](#)]
27. Li, H.; Wu, J.; Wang, L.; Liao, Q.; Niu, X.; Zhang, D.; Wang, K. A zinc ion hybrid capacitor based on sharpened pencil-like hierarchically porous carbon derived from metal-organic framework. *Chem. Eng. J.* **2022**, *428*, 131071. [[CrossRef](#)]
28. Zhao, G.; Han, L.; Ning, K.; Zhu, G.; Yang, J.; Wang, H. O doped Tremella-shaped porous carbon for zinc-ion hybrid capacitors with long life and enhanced energy density. *Mater. Lett.* **2022**, *329*, 133180. [[CrossRef](#)]
29. Chen, C.; Li, P.; Wang, T.; Wang, S.; Zhang, M. S-Doped Carbon Fibers Uniformly Embedded with Ultrasmall TiO₂ for Na⁺/Li⁺ Storage with High Capacity and Long-Time Stability. *Small* **2019**, *15*, e1902201. [[CrossRef](#)]
30. Chen, C.; Yang, Y.; Tang, X.; Qiu, R.; Wang, S.; Cao, G.; Zhang, M. Graphene-Encapsulated FeS₂ in Carbon Fibers as High Reversible Anodes for Na⁺/K⁺ Batteries in a Wide Temperature Range. *Small* **2019**, *15*, e1804740. [[CrossRef](#)]
31. Marpaung, F.; Kim, M.; Khan, J.; Konstantinov, K.; Yamauchi, Y.; Hossain, M.; Na, J.; Kim, J. Metal-Organic Framework (MOF)-Derived Nanoporous Carbon Materials. *Chem. Asian J.* **2019**, *14*, 1331–1343. [[CrossRef](#)] [[PubMed](#)]
32. Mōri, T.; Namba, Y. Crystal structure of diamondlike carbon films prepared by ionized deposition from methane gas. *J. Appl. Phys.* **1984**, *55*, 3276–3279. [[CrossRef](#)]

33. Shao, J.; Zhu, G.; Xie, L.; Tao, S.; Zhang, Y.; Zhang, J.; Wang, H.; Zhang, L.; Chen, C. One-step production of N, S co-doped honeycomb-like activated carbon from instant dry yeast for high gravimetric and volumetric performance supercapacitors. *Diam. Relat. Mater.* **2022**, *127*, 109165. [[CrossRef](#)]
34. Streletskiy, O.; Zavidovskiy, I.; Sychev, V.; Dudin, A.; Savinov, S.; Pavlikov, A. Magnetron deposition of a-C: ND coatings by nanodiamond transfer: Pulse number impact on aggregation and graphitization. *Appl. Phys. A* **2021**, *128*, 1–8. [[CrossRef](#)]
35. Gao, S.; Geng, K.; Liu, H.; Wei, X.; Zhang, M.; Wang, P.; Wang, J. Transforming organic-rich amaranthus waste into nitrogen-doped carbon with superior performance of the oxygen reduction reaction. *Energy Environ. Sci.* **2015**, *8*, 221–229. [[CrossRef](#)]
36. Li, W.; Li, M.; Wang, M.; Zeng, L.; Yu, Y. Electrospinning with partially carbonization in air: Highly porous carbon nanofibers optimized for high-performance flexible lithium-ion batteries. *Nano Energy* **2015**, *13*, 693–701. [[CrossRef](#)]
37. Yun, Y.; Cho, S.; Shim, J.; Kim, B.; Chang, S.; Beak, S.; Huh, Y.; Tak, V.; Park, Y.; Prak, S.; et al. Microporous carbon nanoplates from regenerated silk proteins for supercapacitors. *Adv. Mater.* **2013**, *25*, 1993–1998. [[CrossRef](#)]
38. Schwan, J.; Ulrich, S.; Batori, V.; Ehrhardt, H.; Silva, S. Raman spectroscopy on amorphous carbon films. *J. Appl. Phys.* **1996**, *80*, 440–447. [[CrossRef](#)]
39. Kim, C.; Park, S.; Cho, J.; Lee, D.; Park, T.; Lee, W.; Yang, K. Raman spectroscopic evaluation of polyacrylonitrile-based carbon nanofibers prepared by electrospinning. *J. Raman Spectrosc.* **2004**, *35*, 928–933. [[CrossRef](#)]
40. Fan, H.; Niu, R.; Duan, J.; Liu, W.; Shen, W. Fe₃O₄@Carbon Nanosheets for All-Solid-State Supercapacitor Electrodes. *ACS Appl. Mater. Interfaces* **2016**, *8*, 19475–19483. [[CrossRef](#)]
41. Ma, C.; Li, Y.; Shi, J.; Song, Y.; Liu, L. High-performance supercapacitor electrodes based on porous flexible carbon nanofiber paper treated by surface chemical etching. *Chem. Eng. J.* **2014**, *249*, 216–225. [[CrossRef](#)]
42. Wu, T.; Jing, M.; Yang, L.; Zou, G.; Hou, H.; Zhang, Y.; Zhang, Y.; Cao, X.; Ji, X. Controllable Chain-Length for Covalent Sulfur-Carbon Materials Enabling Stable and High-Capacity Sodium Storage. *Adv. Energy Mater.* **2019**, *9*, 1803478. [[CrossRef](#)]
43. Zhao, G.; Xu, X.; Zhu, G.; Shi, J.; Li, Y.; Zhang, S.; Hossain, M.S.A.; Wu, K.C.-W.; Tang, J.; Yamauchi, Y. Flexible nitrogen-doped carbon heteroarchitecture derived from ZIF-8/ZIF-67 hybrid coating on cotton biomass waste with high supercapacitive properties. *Microporous Mesoporous Mater.* **2020**, *303*, 110257. [[CrossRef](#)]
44. Olabi, A.G.; Abbas, Q.; Abdelkareem, M.; Alami, A.H.; Mirzaeian, M.; Sayed, E.T. Carbon-based materials for supercapacitors: Recent progress, challenges and barriers. *Batteries* **2023**, *9*, 19. [[CrossRef](#)]
45. Xia, J.; Zhang, N.; Chong, S.; Li, D.; Chen, Y.; Sun, C. Three-dimensional porous graphene-like sheets synthesized from biocarbon via low-temperature graphitization for a supercapacitor. *Green Chem.* **2018**, *20*, 694–700. [[CrossRef](#)]
46. Xu, B.; Wang, H.; Zhu, Q.; Sun, N.; Anasori, B.; Hu, L.; Wang, F.; Guan, Y.; Gogotsi, Y. Reduced graphene oxide as a multi-functional conductive binder for supercapacitor electrodes. *Energy Storage Mater.* **2018**, *12*, 128–136. [[CrossRef](#)]
47. Li, Q.; Xie, W.; Liu, D.; Wang, Q.; He, D. Nitrogen and oxygen co-doped carbon nanofibers with rich sub-nanoscale pores as self-supported electrode material of high-performance supercapacitors. *Electrochim. Acta* **2016**, *222*, 1445–1454. [[CrossRef](#)]
48. Chen, L.; Lu, Y.; Yu, L.; Lou, X. Designed formation of hollow particle-based nitrogen-doped carbon nanofibers for high-performance supercapacitors. *Energy Environ. Sci.* **2017**, *10*, 1777–1783. [[CrossRef](#)]
49. Cheng, H.; Chen, X.; Yu, H.; Guo, M.; Chang, Y.; Zhang GHierarchically Porous, N, P-Codoped Carbon Materials for High-Performance Supercapacitors. *ACS Appl. Energy Mater.* **2020**, *3*, 10080–10088. [[CrossRef](#)]
50. He, H.; Lian, J.; Chen, C.; Xiong, Q.; Zhang, M. Super hydrophilic carbon fiber film for freestanding and flexible cathodes of zinc-ion hybrid supercapacitors. *Chem. Eng. J.* **2021**, *421*, 129786. [[CrossRef](#)]
51. Jiang, C.; Zou, Z. Waste polyurethane foam filler-derived mesoporous carbons as superior electrode materials for EDLCs and Zn-ion capacitors. *Diam. Relat. Mater.* **2020**, *101*, 107603. [[CrossRef](#)]
52. Liu, Y.; Tan, H.; Tan, Z.; Cheng, X. Rice husk-derived carbon materials for aqueous Zn-ion hybrid supercapacitors. *Appl. Surf. Sci.* **2023**, *608*, 155215.
53. Wang, H.; Huang, J.; Wang, X.; Guo, Z.; Liu, W. Fabrication of TiN/CNTs on carbon cloth substrates via a CVD–ALD method as free-standing electrodes for zinc ion hybrid capacitors. *New J. Chem.* **2022**, *46*, 15175–15184. [[CrossRef](#)]
54. Wang, Q.; Wang, S.; Guo, X.; Ruan, L.; Wei, N.; Ma, Y.; Li, J.; Wang, M.; Li, W.; Zeng, W. MXene-Reduced Graphene Oxide Aerogel for Aqueous Zinc-Ion Hybrid Supercapacitor with Ultralong Cycle Life. *Adv. Electron. Mater.* **2019**, *5*, 1900537. [[CrossRef](#)]
55. Zhu, Y.; Ye, X.; Jiang, H.; Xie, J.; Yue, Z.; Wang, L.; Wan, Z.; Jia, C.; Yao, X. Controlled swelling of graphene films towards hierarchical structures for supercapacitor electrodes. *J. Power Sources* **2020**, *453*, 227851. [[CrossRef](#)]
56. Chen, S.; Ma, L.; Zhang, K.; Kamruzzaman, M.; Zhi, C.; Zapien, J.A. A flexible solid-state zinc ion hybrid supercapacitor based on co-polymer derived hollow carbon spheres. *J. Mater. Chem. A* **2019**, *7*, 7784–7790. [[CrossRef](#)]
57. Jian, Z.; Yang, N.; Vogel, M.; Leith, S.; Schulte, A.; Schönher, H.; Jiao, T.; Zhang, W.; Müller, J.; Butz, B.; et al. Flexible Diamond Fibers for High-Energy-Density Zinc-Ion Supercapacitors. *Adv. Energy Mater.* **2020**, *10*, 2002202.

Disclaimer/Publisher’s Note: The statements, opinions and data contained in all publications are solely those of the individual author(s) and contributor(s) and not of MDPI and/or the editor(s). MDPI and/or the editor(s) disclaim responsibility for any injury to people or property resulting from any ideas, methods, instructions or products referred to in the content.